SIGNAL ANALYSIS OF APERTURELESS SCANNING NEAR-FIELD OPTICAL MICROSCOPY WITH SUPERLENS

C.-H. Chuang and Y.-L. Lo [†]

Department of Mechanical Engineering
National Cheng Kung University, Tainan 701, Taiwan

Abstract—Apertureless scanning near-field optical microscopy (A-SNOM) with a superlens is a novel nano-optical system for sub-wavelength imaging purposes. This study presents a quantitative model for analyzing the heterodyne signals obtained from an A-SNOM fitted with a superlens at various harmonics of the AFM tip vibration frequency. It is shown that the image resolution is determined not only by the tip radius, but also by the superlens transmission coefficient in the high evanescent wave vector K_x. Moreover, the analytical results show that the images acquired from the A-SNOM/superlens system are adversely affected by a signal contrast problem as a result of the noise generated by the tip-superlens interaction electric field. However, it is shown that this problem can be easily resolved using a background noise compensation method, thereby resulting in a significant improvement in the signal-to-background (S/B) ratio. The feasibility of utilizing the system for maskless nanolithography applications is discussed. It is shown that the A-SNOM/superlens system in nanolithography yields a dramatic improvement in the signal intensity and S/B ratio compared to that of a conventional A-SNOM with a bare tip only.

1. INTRODUCTION

Near-field scanning optical microscopy (SNOM) is a mature technology for obtaining nano-resolution images [1, 2]. In SNOM, a nano-aperture tip in the form of a tapered optical fiber coated with metal is scanned across the surface of interest by a positioning stage with nanometer

positioning accuracy in order to investigate the optical near-field. The SNOM tip has a typical aperture diameter of around 50–100 nm [3] and is attached to a dither piezo which induces a vibration of the tip at its resonance frequency. However, the tip aperture limits both the image resolution and the light throughput, and thus apertureless SNOM (A-SNOM) [4–6], in which resolutions of better than 10 nm can be obtained, has emerged as the method of choice for sub-wavelength imaging applications in recent years. In A-SNOM, the tip enhances the external field and simultaneously serves as an efficient antenna [7]. Consequently, a significant improvement in the tip-sample optical coupling is obtained relative to that in conventional SNOM. However, the performance improvement of A-SNOM is obtained at the expense of considerably more complex signal processing [4–6].

Superlenses were first presented by Pendry [8], who showed that materials with a negative refractive index (NRI) [9–13] have the ability to amplify evanescent waves. Various researchers have demonstrated the ability of superlenses to obtain nano-resolution images in the near-field [14, 15]. Furthermore, Taubner et al. [16] fitted an A-SNOM with a $SiO_2/SiC/SiO_2$ superlens/sample and showed that the system made possible the indirect access of optical images via a near-field scanning probe. However, the spatial resolution of the A-SNOM/superlens system was found to be poorer than that of a conventional A-SNOM.

In previous studies, Chuang and Lo [17, 18] presented analytical models for analyzing the homodyne and heterodyne signals of a general A-SNOM system. The results showed that the signal-to-background (S/B) ratio in such systems could be improved by increasing the wavelength of the incident light or reducing its angle of incidence. In addition, it was shown that a higher S/B ratio could be obtained by using a phase modulation depth of over 1 or a tip vibration with a ramp function. However, no such models currently exist for the quantitative analysis of the detection signals in an A-SNOM fitted with a superlens.

Accordingly, the present study develops a comprehensive interference-based model for analyzing the amplitude and phase of the heterodyne detection signal in an A-SNOM/superlens system at various harmonics of the tip vibration frequency. The limitations of quasi-electrostatic theory in modeling the tip-superlens interaction are also discussed. It is shown that the spatial resolution of an A-SNOM fitted with a superlens depends not only on the tip radius, but also on the superlens transmission coefficient in the high evanescent wave vector K_x. In addition, it was shown that the resolution of the superlens is strongly suppressed even for small absorption [19]. Moreover, the results show that the image contrast and S/B ratio are degraded by the background noise generated by the tip-superlens

enhancement electric field. However, it is shown that both the signal contrast and the S/B ratio can be dramatically improved via the use of a background noise compensation method. Finally, the feasibility of utilizing the system for accomplishing nanolithography applications is explored and discussed.

2. ELECTRIC FIELDS IN HETERODYNE A-SNOM WITH SUPERLENS

In interferometer-type A-SNOMs [4, 18, 20], a generic frequency shifting device such as an acousto-optic modulator (AOM) is used to add a radian shifting frequency $\Delta\omega$ to the reference beam. Consequently, the reference beam can be modeled as

$$\vec{\mathbf{E}}_{Reference} = E_R e^{i((\omega + \Delta\omega)t + \phi_R)}, \tag{1}$$

where ω is the radian frequency of the incident light and E_R and Φ_R are the amplitude and initial phase of the reference beam, respectively.

Figure 1 shows an enlarged view of the near-field region in an A-SNOM fitted with a superlens. In the A-SNOM scanning procedure,
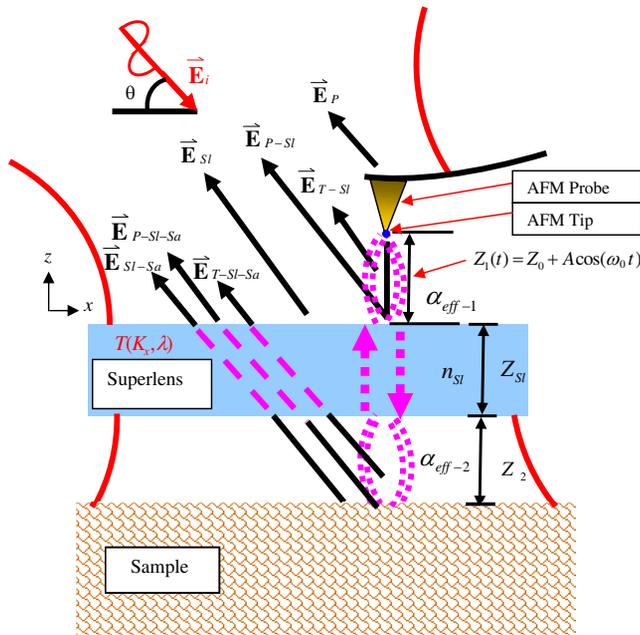

Figure 1. Detailed view of near-field region in A-SNOM with a superlens.

the AFM drives the tip with a vertical cosine vibration around a mean position Z_0. Assuming that the amplitude and radian frequency of the tip vibration are denoted as A and ω_0, respectively, the dynamic variation of the tip position over time can be written as

$$Z_1(t) = Z_0 + A\cos(\omega_0 t). \tag{2}$$

Note that in the figure, the word "tip" denotes the tip apex, which interacts with the superlens, while the word "probe" denotes the elongated AFM probe, which creates an unwanted background scattering effect. As shown, the incident electric field, $\vec{\mathbf{E}}_i$, strikes the superlens with an angle θ and produces seven different electromagnetic waves, namely (1) an interaction electric field $\vec{\mathbf{E}}_{T-Sl}$ between the AFM tip and the superlens; (2) an interaction electric field $\vec{\mathbf{E}}_{T-Sl-Sa}$ between the tip-superlens enhancement dipole passing through the superlens and the sample; (3) an electric field $\vec{\mathbf{E}}_P$ scattered directly from the AFM probe; (4) an electric field $\vec{\mathbf{E}}_{P-Sl}$ scattered from the AFM probe and then reflected from the superlens surface; (5) an electric field $\vec{\mathbf{E}}_{P-Sl-Sa}$ scattered from the AFM probe and then reflected from the sample surface through the superlens; (6) an electric field $\vec{\mathbf{E}}_{Sl}$ scattered directly from the superlens; and (7) an electric field $\vec{\mathbf{E}}_{Sl-Sa}$ scattered from the sample through the superlens.

In the current analysis, it is assumed that all the incident light and detected light passes through the objective lens. Furthermore, for the sake of simplicity, an assumption is made that the background scattering electric fields from the AFM probe, superlens and sample, respectively, are weakly scattered from multiple points. The series of scattering fields from these single points can be truncated at the first order of dielectric susceptibility. Thus, these background scattering electric fields described by Green's tensors become identity tensors [21]. Accordingly, the present analysis utilizes quasi-electrostatic theory [4–6] to describe the tip-sample interaction with effective polarizability. Note that since the TE wave component in the tip-sample enhancement field is relatively weak in A-SNOM systems [5], the analysis focuses specifically on the TM polarization incident light within the A-SNOM/superlens system.

The first field of interest in an A-SNOM with a superlens is that produced by the interaction between the AFM tip and the superlens, i.e.,

$$\vec{\mathbf{E}}_{T-S1} = \alpha_{eff-1} E_i e^{i(\omega t + \phi_{T-Sl})} \equiv E_{T-Sl} e^{i(\omega t + \phi_{T-Sl})}, \tag{3}$$

where E_i is the amplitude of the incident electric field, α_{eff-1} is the effective polarizability between the tip and the superlens, and

Φ_{T-Sl} is the initial phase of the interaction light. According to quasi-electrostatic theory [4–6], a scattering AFM tip with radius a induces a point polarizablity effect with isotropic polarizablility α at a distance $z = r - a$ above the superlens (where r is the distance from the AFM tip dipole center to the superlens surface). Given an incident electric field E_i, the AFM tip becomes polarized with a dipole moment $p = \alpha E_i$ (where $\alpha = 4\pi a^3(\varepsilon_{tip} - 1)/(\varepsilon_{tip} + 2)$ and ε_{tip} is the complex dielectric number of the AFM tip [22]). For the case in which E_i is perpendicular to the superlens surface, the electric field of the induced tip dipole results in an image dipole moment of $p' = \beta p$ ($\beta_{superlens} = (\varepsilon_{superlens} - 1)/(\varepsilon_{superlens} + 1)$ [22]), located within the superlens at a distance $2r$ from the center of the tip dipole. (Note that $\varepsilon_{superlens}$ is the complex dielectric number of the superlens). The incident field at the tip dipole is enhanced by this image field, and thus the actual tip dipole moment becomes $p = \alpha_{eff-1} E_i$ ($\alpha_{eff-1} = \alpha(1 + \beta_{superlens})/(1 - \alpha\beta_{superlens}/16\pi r^3)$) [4].

There are many kinds of meta-material have superlens phenomenon. For the case of a perfect superlens presented by Pendry [8] with $\varepsilon_{superlens} = -1$ (i.e., no imaginary part), the probe should be close to the superlens surface since the power scattered by the probe can not be infinite. In this special case, the effective polarizability α_{eff-1} can only be simulated using a numerical method such as the finite difference time domain (FDTD) method [23–25]. In other words, a simple analytical solution based upon quasi-electrostatic theory can not be obtained. Furthermore, if $Z_{Sl} \doteq Z_1(t)$, the image dipole cannot be found using the method of images [22]. Note that Z_{Sl} is the superlens thickness. Thus, quasi-electrostatic theory once again fails. Consequently, in utilizing quasi-electrostatic theory to construct the analytical model proposed in this study, it is assumed that the permittivity of the superlens, $\varepsilon_{superlens}$, is not equal to -1 and that $Z_{Sl} \gg Z_1(t)$ and $Z_{Sl} \gg a$.

Of all the electric fields within the A-SNOM/superlens system, $\vec{\mathbf{E}}_{T-Sl-Sa}$, i.e., the interaction electric field between the tip-superlens enhancement dipole passing through the superlens ($\vec{\mathbf{E}}_{T-Sl}$) and the sample, is one of the most important since it is the only near-field measurement signal within the A-SNOM system. $\vec{\mathbf{E}}_{T-Sl-Sa}$ can be written as

$$\vec{\mathbf{E}}_{T-Sl-Sa} = \alpha_{eff-2} T^2(K_{x(T-Sl)}, \lambda) E_i e^{i(\omega t + \phi_{T-Sl})} e^{i(2K\sin(\theta)(n_{Sl}Z_{Sl}+Z_2))}$$

$$\equiv E_{T-Sl-Sa} e^{i(\omega t + \phi_{T-Sl-Sa})}, \tag{4}$$

where $T(K_{x(T-Sl)}, \lambda)$ is the transmission coefficient through the superlens of wave vector $K_{x(T-Sl)}$ of the tip-superlens interaction electric dipole at an incident wavelength λ along the x-axis.

Furthermore, K, defined as $2\pi/\lambda$, is the wave number of the incident light and n_{Sl} is the effective refractive index of the superlens. $Z_2(t)$ is the distance between superlens and sample. In addition, α_{eff-2} is the effective polarizablility between the tip through the superlens and the sample, and can be expressed as $\alpha_{eff-2} = \alpha_{eff-1}(1 + \beta_{sample})$ using the method of images with $\beta_{sample} = (\varepsilon_{sample} - 1)/(\varepsilon_{sample} + 1)$ [22]. It is assumed that the superlnes and the sample are flat; therefore, the other nano-optical phenomena would be not induced. In addition, the refractive index (n_{Sl}) and distances (Z_{Sl} and Z_2) in Eq. (4) remain constant during A-SNOM scanning, and thus the initial phases are all merged within $\phi_{T-Sl-Sa}$. In Eq. (4), the transmission coefficient term can be written as [15, 19]

$$T(K_{x(T-Sl)}, \lambda) = (|E|_{img(T-Sl)}/|E|_{obj(T-Sl)}). \tag{5}$$

In other words, $T(K_{x(T-Sl)}, \lambda)$ is the ratio of the image field ($|E|_{img(T-Sl)}$) to the object field ($|E|_{obj(T-Sl)}$) of the interaction electric dipole between the tip and the superlens. It was shown in [19] that in a lossless media, any deviation of the complex dielectric number, ε, from -1 causes a significant reduction in the resolution of a superlens. If $|K_x| > |K|$ ($K = 2\pi/\lambda$), K_x represents an evanescent wave [8]. The transmission coefficient formulas of superlens transmission properties can be found in Refs. [8, 26, 27]. In order to simplify the analysis in this study, the superlens transmission coefficients can generically vary from 0% to 100%. However, it should be noted that long wavelength superlenses generally have a poor spatial resolution due to the high magnitude of the wave vector $K_{x(T-Sl)}$ of the tip enhancement electric field. As a result, the spatial resolution of an A-SNOM fitted with a superlens [16] is poorer than that of a conventional A-SNOM [3–5, 20].

In the present analysis, it is assumed that the AFM probe does not perturb the near-field region (i.e., as also assumed in [28]). Consequently, the third field of interest in the A-SNOM/superlens system, i.e., the electric field scattered from the probe, can be formulated as

$$\vec{\mathbf{E}}_P = E_P e^{i(\omega t + \phi_P)} e^{i(2K \sin(\theta) Z_1(t))}, \tag{6}$$

where E_P and Φ_P are the amplitude and initial phase of the scattering electric field from the probe, respectively, and $e^{i(2K \sin(\theta) Z_1(t))}$ represents the phase vibration caused by the vertical dither of the probe.

The fourth electric field, $\vec{\mathbf{E}}_{P-Sl}$, of interest in the A-SNOM/superlens system is the electric field that reflects the electric field $\vec{\mathbf{E}}_P$ from the superlens. From Fig. 1, it can be seen that the optical

path difference between the direct AFM scattering electric field and the superlens scattering field reflected from the AFM probe is equivalent to $2K\sin(\theta)Z_1(t)$. Therefore, the reflected superlens scattering field can be formulated as

$$
\begin{aligned}
\vec{\mathbf{E}}_{P-Sl} &= E_{P-Sl}e^{i(\omega t+\phi_P+2K\sin(\theta)Z_1(t))}e^{i(2K\sin(\theta)Z_1(t))}\\
&= E_{P-Sl}e^{i(\omega t+\phi_P)}e^{i(4K\sin(\theta)Z_1(t))}.
\end{aligned}
\tag{7}
$$

The fifth electric field in the A-SNOM/superlens near-field system is that scattered from the AFM probe and then reflected from the sample surface through the superlens. This field can be expressed as

$$
\begin{aligned}
&\vec{\mathbf{E}}_{P-Sl-Sa}\\
&= E_{P-Sl}T^2(K_{x(P)},\lambda)e^{i(2K\sin(\theta)(n_{Sl}Z_{Sl}+Z_2))}e^{i(\omega t+\phi_P)}e^{i(4K\sin(\theta)Z_1(t))}\\
&\equiv E_{P-Sl-Sa}e^{i(\omega t+\phi_{P-Sl-Sa})}e^{i(4K\sin(\theta)Z_1(t))},
\end{aligned}
\tag{8}
$$

where $T(K_{x(P)},\lambda)$ is the transmission coefficient through the superlens of the probe scattering electric field with wavelength λ. Unlike $T(K_{x(T-Sl)},\lambda)$, $T(K_{x(P)},\lambda)$ is related to the probe without any nano-spatial information, therefore it can be treated as the regular medium transmission coefficient. In Eq. (8), electric fields $\vec{\mathbf{E}}_{P-Sl}$ and $\vec{\mathbf{E}}_{P-Sl-Sa}$ have the same $4K\sin(\theta)Z_1(t)$ and light radian frequency ω features, and can therefore be combined as follows:

$$
\begin{aligned}
&\vec{\mathbf{E}}_{P-Sl} + \vec{\mathbf{E}}_{P-Sl-Sa} = \vec{\mathbf{E}}_{(P-Sl)+(P-Sl-Sa)}\\
&= E_{(P-Sl)+(P-Sl-Sa)}e^{i(\omega t+\phi_{(P-Sl)+(P-Sl-Sa)})}e^{i(4K\sin(\theta)Z_1(t))}.
\end{aligned}
\tag{9}
$$

The sixth electric field in the near-field region is that of the light scattered directly from the superlens surface. Since this electric field is not modulated by the AFM probe vibration, it can be expressed simply as

$$
\vec{\mathbf{E}}_{Sl} = E_{Sl}e^{i(\omega t+\phi_{Sl})},
\tag{10}
$$

where E_{Sl} and Φ_{Sl} are the amplitude and initial phase of the scattering light from the superlens surface, respectively.

The final electric field of interest in the A-SNOM/superlens system is that scattered from the sample through the superlens. This field can be expressed as

$$
\begin{aligned}
\vec{\mathbf{E}}_{Sl-Sa} &= E_{Sl}T^2(K_{x(Sl-Sa)},\lambda)e^{i(\omega t+\phi_P)}e^{i(2K\sin(\theta)(n_{Sl}Z_{Sl}+Z_2))}\\
&\equiv E_{Sl-Sa}e^{i(\omega t+\phi_{Sl-Sa})},
\end{aligned}
\tag{11}
$$

where $T(K_{x(Sl-Sa)},\lambda)$ is the transmission coefficient through the superlens of the sample scattering electric field with wavelength λ.

As with $T(K_{x(P)}, \lambda)$, $T(K_{x(Sl-Sa)}, \lambda)$ is related to the sample without any nano-spatial information, therefore it can be treated as the regular medium transmission coefficient. Furthermore, electric fields $\vec{\mathbf{E}}_{Sl}$ and $\vec{\mathbf{E}}_{Sl-Sa}$ have the same features, and can therefore be combined as follows:

$$\vec{\mathbf{E}}_{Sl} + \vec{\mathbf{E}}_{Sl-Sa} = \vec{\mathbf{E}}_{(Sl)+(Sl-Sa)} = E_{(Sl)+(Sl-Sa)}e^{i(\omega t+\phi_{(Sl)+(Sl-Sa)})}. \quad (12)$$

3. ANALYTICAL MODEL OF HETERODYNE DETECTION SIGNAL IN A-SNOM WITH SUPERLENS

The total electric field entering the A-SNOM system is equivalent to the sum of the reference beam and the seven electric fields described in the previous section, i.e.,

$$\begin{aligned}
\vec{\mathbf{E}}_{Total} &= \vec{\mathbf{E}}_{Reference} + \vec{\mathbf{E}}_{T-Sl} + \vec{\mathbf{E}}_{T-Sl-Sa} \\
&+ \vec{\mathbf{E}}_P + \vec{\mathbf{E}}_{(P-Sl)+(P-Sl-Sa)} + \vec{\mathbf{E}}_{(Sl)+(Sl-Sa)} \quad (13)
\end{aligned}$$

The corresponding intensity signal, $I(t)$, is given by

$$I(t) = I_{hom}(t) + I_{het}(t). \quad (14)$$

Heterodyne detection has a better S/B ratio than that of homodyne detection [18], and thus the present analysis focuses specifically on the heterodyne intensity component, $I_{het}(t)$, within the detected intensity signal $I(t)$. In developing the analytical model of the A-SNOM/superlens system, the heterodyne signal is formulated as

$$\begin{aligned}
I_{het}(t) = {} & E_R^2 \\
& + 2E_R E_{T-Sl} \cos(\Delta\omega t + \phi_R - \phi_{T-Sl}) \\
& + 2E_R E_{T-Sl-Sa} \cos(\Delta\omega t + \phi_R - \phi_{T-Sl-Sa}) \\
& + 2E_R E_P \cos(\Delta\omega t + \phi_R - \phi_P - 2K\sin(\theta)Z_0 - 2K\sin(\theta)A\cos(\omega_0 t)) \\
& + 2E_R E_{(P-Sl)+(P-Sl-Sa)} \cos(\Delta\omega t + \phi_R - \phi_{(P-Sl)+(P-Sl-Sa)} \\
& - 4K\sin(\theta)Z_0 - 4K\sin(\theta)A\cos(\omega_0 t)) \\
& + 2E_R E_{(Sl)+(Sl-Sa)} \cos(\Delta\omega t + \phi_R - \phi_{(Sl)+(Sl-Sa)}). \quad (15)
\end{aligned}$$

Applying the Fourier Bessel series expansion [29], and introducing the phase differences $\psi_1 = \Phi_R - \Phi_P - 2k\sin(\theta)Z_0$ and $\psi_2 = \Phi_R - \Phi_{(P-Sl)+(P-Sl-Sa)} - 4k\sin(\theta)Z_0$ and the phase modulation depth $\psi_3 =$

$2K\sin(\theta)A$, Eq. (15) can be rewritten in the form

$$I_{het}(t) = E_R^2$$
$$+2E_R E_{T-Sl}\cos(\phi_R - \phi_{T-Sl} + \Delta\omega t)$$
$$+2E_R E_{T-Sl-Sa}\cos(\phi_R - \phi_{T-Sl-Sa} + \Delta\omega t)$$
$$+2E_R E_P\left\{\left[J_0(\psi_3) + 2\sum_{j=1}^{\infty}(-1)^j J_{2j}(\psi_3)\cos(2j\omega_0 t)\right]\cos(\Delta\omega t + \psi_1)\right.$$
$$\left.+2\sum_{j=0}^{\infty}(-1)^j J_{2j+1}(\psi_3)\cos[(2j+1)\omega_0 t]\sin(\Delta\omega t + \psi_1)\right\}$$
$$+2E_R E_{(P-Sl)+(P-Sl-Sa)}\left\{\left[J_0(2\psi_3)\right.\right.$$
$$+2\sum_{j=1}^{\infty}(-1)^j J_{2j}(2\psi_3)\cos(2j\omega_0 t)\right]\cos(\Delta\omega t + \psi_2)$$
$$+2\sum_{j=0}^{\infty}(-1)^j J_{2j+1}(2\psi_3)\cos[(2j+1)\omega_0 t]\sin(\Delta\omega t + \psi_2)\right\}$$
$$+2E_R E_{(Sl)+(Sl-Sa)}\cos(\phi_R - \phi_{(Sl)+(Sl-Sa)} + \Delta\omega t), \qquad (16)$$

where $J_n(\psi_3)$ and $J_n(2\psi_3)$ are n-th order Bessel functions of the first kind at phase modulation depths ψ_3 and $2\psi_3$, respectively. In Eq. (16), the higher-order background electric field signals in $E_R E_P$ and $E_R E_{(P-Sl)+(P-Sl-Sa)}$ decay rapidly as the modulation depth, ψ_3, approaches zero [17, 18]. Since the amplitude of the interaction electric field between the tip and the superlens varies nonlinearly as the tip vibrates, an assumption is made that E_{T-Sl} can be expressed as the sum of the individual components oscillating at various harmonics of the AFM tip modulation radian frequency [30], i.e.,

$$E_{T-Sl} = E_{T-Sl}^{0\omega_0}$$
$$+E_{T-Sl}^{1\omega_0}\cos(\omega_0 t) + E_{T-Sl}^{2\omega_0}\cos(2\omega_0 t) + E_{T-Sl}^{3\omega_0}\cos(3\omega_0 t) + \dots \quad (17)$$

Furthermore, $E_{T-Sl-Sa}$ becomes

$$E_{T-Sl-Sa} = \alpha_{eff-2}T^2(K_{x(T-Sl)}, \lambda)(E_{T-Sl}^{0\omega_0} + E_{T-Sl}^{1\omega_0}\cos(\omega_0 t)$$
$$+E_{T-Sl}^{2\omega_0}\cos(2\omega_0 t) + E_{T-Sl}^{3\omega_0}\cos(3\omega_0 t) + \dots). \quad (18)$$

Note that the series coefficients $E_{T-Sl}^{n\omega_0}$ in Eq. (17) can be obtained from the Fourier components of $E_i\alpha_{eff-1}$. Substituting Eqs. (17) and (18) into Eq. (16), the heterodyne intensity $I_{het}(t)$ signal can be

reformulated as

$$I_{het}(t) = E_R^2$$

$$+2\sum_{n=0}^{\infty} E_{T-Sl}^{n\omega_0} \cos(n\omega_0 t) E_R \cos(\phi_R - \phi_{T-Sl} + \Delta\omega t)$$

$$+2\sum_{n=0}^{\infty} \alpha_{eff-2} T^2(K_{x(T-Sl)}, \lambda) E_1^{n\omega_0} \cos(n\omega_0 t) E_R$$

$$\cos(\phi_R - \phi_{T-Sl-Sa} + \Delta\omega t)$$

$$+2E_R E_P \left\{ \left[J_0(\psi_3) + 2\sum_{j=1}^{\infty} (-1)^j J_{2j}(\psi_3) \cos(2j\omega_0 t) \right] \cos(\Delta\omega t + \psi_1) \right.$$

$$+2\sum_{j=0}^{\infty} (-1)^j J_{2j+1}(\psi_3) \cos[(2j+1)\omega_0 t] \sin(\Delta\omega t + \psi_1) \right\}$$

$$+2E_R E_{(P-Sl)+(P-Sl-Sa)} \left\{ \left[J_0(2\psi_3) \right. \right.$$

$$+2\sum_{j=1}^{\infty} (-1)^j J_{2j}(2\psi_3) \cos(2j\omega_0 t) \right] \cos(\Delta\omega t + \psi_2)$$

$$+2\sum_{j=0}^{\infty} (-1)^j J_{2j+1}(2\psi_3) \cos[(2j+1)\omega_0 t] \sin(\Delta\omega t + \psi_2) \right\}$$

$$+2E_R E_{(Sl)+(Sl-Sa)} \cos(\phi_R - \phi_{(Sl)+(Sl-Sa)} + \Delta\omega t). \tag{19}$$

Rearranging Eq. (19) in order of the modulation radian frequency, i.e., $\Delta\omega + n\omega_0$, the heterodyne intensity signal can be expressed in terms of the following components:

$$I_{het}(t) = E_R^2 \ldots DC$$

$$2E_{T-Sl}^{0\omega_0} E_R \cos(\phi_R - \phi_{T-Sl} + \Delta\omega t)$$

$$+2\alpha_{eff-2} T^2(K_{x(T-Sl)}, \lambda) E_{T-Sl-Sa}^{0\omega_0} E_R \cos(\phi_R - \phi_{T-Sl-Sa} + \Delta\omega t)$$

$$+2E_R E_P J_0(\psi_3) \cos(\Delta\omega t + \psi_1)$$

$$+2E_R E_{(P-Sl)+(P-Sl-Sa)} J_0(2\psi_3) \cos(\Delta\omega t + \psi_2)$$

$$+2E_{(Sl)+(Sl+Sa)} E_R \cos(\phi_R - \phi_{(Sl)+(Sl-Sa)} + \Delta\omega t) \ldots \Delta\omega$$

$$+4E_R E_P J_1(\psi_3) \cos(\omega_0 t) \sin(\Delta\omega t + \psi_1)$$

$$+4E_R E_{(P-Sl)+(P-Sl-Sa)} J_1(2\psi_3) \cos(\omega_0 t) \sin(\Delta\omega t + \psi_2)$$

$$+2E_{T-Sl}^{1\omega_0} E_R \cos(\omega_0 t) \cos(\phi_R - \phi_{T-Sl} + \Delta\omega t)$$

$$+2\alpha_{eff-2} T^2(K_{x(T-Sl)}, \lambda) E_{T-Sl}^{1\omega_0} E_R \cos(\omega_0 t)$$

$$\cos(\phi_R - \phi_{T-Sl-Sa} + \Delta\omega t) \ldots (\Delta\omega \pm 1\omega_0)t$$

$$-4E_R E_P J_2(\psi_3) \cos(2\omega_0 t) \cos(\Delta\omega t + \psi_1)$$

$$-4E_R E_{(P-Sl)+(P-Sl-Sa)} J_2(2\psi_3) \cos(2\omega_0 t) \cos(\Delta\omega t + \psi_2)$$

$$+2E_{T-Sl}^{2\omega_0} E_R \cos(2\omega_0 t) \cos(\phi_R - \phi_{T-Sl} + \Delta\omega t)$$

$$+2\alpha_{eff-2} T^2(K_{x(T-Sl)}, \lambda) E_1^{2\omega_0} E_R \cos(2\omega_0 t)$$

$$\cos(\phi_R - \phi_{T-Sl-Sa} + \Delta\omega t) \ldots (\Delta\omega \pm 2\omega_0)t$$

$$-4E_R E_P J_3(\psi_3) \cos(3\omega_0 t) \sin(\Delta\omega t + \psi_1)$$

$$-4E_R E_{(P-Sl)+(P-Sl-Sa)} J_3(2\psi_3) \cos(3\omega_0 t) \sin(\Delta\omega t + \psi_2)$$

$$+2E_{T-Sl}^{3\omega_0} E_R \cos(3\omega_0 t) \cos(\phi_R - \phi_{T-Sl} + \Delta\omega t)$$

$$+2\alpha_{eff-2} T^2(K_{x(T-Sl)}, \lambda) E_{T-Sl}^{3\omega_0} E_R \cos(3\omega_0 t)$$

$$\cos(\phi_R - \phi_{T-Sl-Sa} + \Delta\omega t) \ldots (\Delta\omega \pm 3\omega_0)t$$

$$+4E_R E_P J_4(\psi_3) \cos(4\omega_0 t) \cos(\Delta\omega t + \psi_1)$$

$$+4E_R E_{(P-Sl)+(P-Sl-Sa)} J_4(2\psi_3) \cos(4\omega_0 t) \cos(\Delta\omega t + \psi_2)$$

$$+2E_{T-Sl}^{4\omega_0} E_R \cos(4\omega_0 t) \cos(\phi_R - \phi_{T-Sl} + \Delta\omega t)$$

$$+2\alpha_{eff-2} T^2(K_{x(T-Sl)}, \lambda) E_{T-Sl}^{4\omega_0} E_R \cos(4\omega_0 t)$$

$$\cos(\phi_R - \phi_{T-Sl-Sa} + \Delta\omega t) \ldots (\Delta\omega \pm 4\omega_0)t$$

$$+2E_R E_P \left\{ 2\sum_{j=3}^{\infty} (-1)^j J_{2j}(\psi_3) \cos(2j\omega_0 t) \cos(\Delta\omega t + \psi_1) \right.$$

$$\left. +2\sum_{j=2}^{\infty} (-1)^j J_{2j+1}(\psi_3) \cos[(2j+1)\omega_0 t] \sin(\Delta\omega t + \psi_1) \right\}$$

$$+2E_R E_{(P-Sl)+(P-Sl-Sa)} \left\{ 2\sum_{j=3}^{\infty} (-1)^j J_{2j}(\psi_3) \cos(2j\omega_0 t) \cos(\Delta\omega t + \psi_1) \right.$$

$$\left. +2\sum_{j=2}^{\infty} (-1)^j J_{2j+1}(\psi_3) \cos[(2j+1)\omega_0 t)] \sin(\Delta\omega t + \psi_1) \right\}$$

$$+2\sum_{n=5}^{\infty} E_{T-Sl}^{n\omega_0} E_R \cos(n\omega_0 t) \cos(\phi_R - \phi_{T-Sl} + \Delta\omega t)$$

$$+2\sum_{n=5}^{\infty} \alpha_{eff-2} T^2(K_{x(T-Sl)}, \lambda) E_{T-Sl}^{n\omega_0} E_R$$

$$\cos(n\omega_0 t) \cos(\phi_R - \phi_{T-Sl-Sa} + \Delta\omega t) \tag{20}$$

Equation (20) shows the fundamental characteristics of the

heterodyne intensity signal of an A-SNOM system fitted with a superlens. The equation shows that it is impossible to acquire the absolute interaction electric field $\vec{\mathbf{E}}_{T-Sl-Sa}$. However, the intensities of the background electric fields $E_R E_P$ and $E_R E_{(P-Sl)+(P-Sl-Sa)}$ have coefficients of $J_n(\psi_3)$ and $J_n(2\psi_3)$, respectively. As a result, if the higher-order coefficients of these background electric fields decay more rapidly than those of the $E_{T-Sl}^{n\omega_0}$ signal, the lock-in detection signal will exhibit an improved signal contrast when applied to different samples at higher orders of the harmonic modulation radian frequency.

4. SIMULATION OF A-SNOM WITH COMPOSITE SUPERLENS/SAMPLE

Figure 2 shows the A-SNOM system with a composite superlens/sample in the near-field region considered previously in [16]. It is noticed that the analytical model presented in this study just adopts a general case of superlens with transmission coefficient $T(K_{x(T-Sl)}, \lambda)$ instead of the specific $SiO_2/SiC/SiO_2$ superlens used in [16]. As shown, the sample comprises two different materials, designated as S_1 and S_2, respectively. When the gap Z_2 between the superlens and the sample is equal to zero, the model has no secondary enhancement effect,
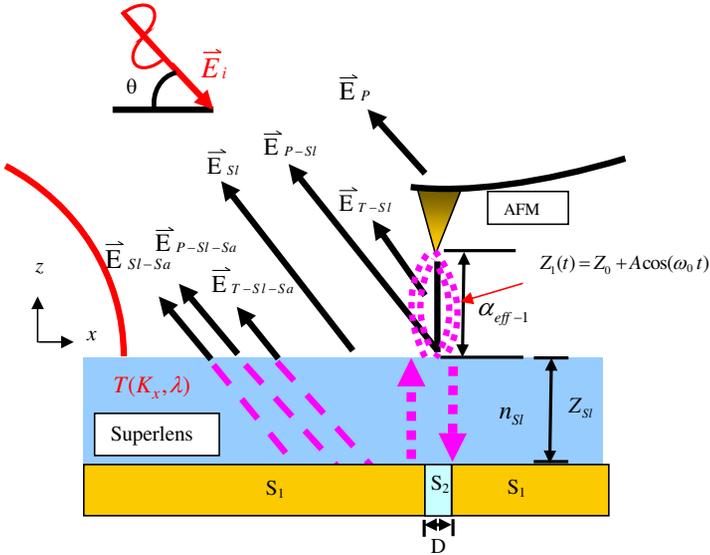

Figure 2. A-SNOM with composite superlens/sample in near-field region.

and thus the term α_{eff-2} in Eq. (20). is replaced by a reflectance at the interface between the superlens and the sample (see Fig. 2). Assume that the reflectances from samples S_1 and S_2 are 90% and 10%, respectively. Accordingly, the ideal measurement signal contrast between the two specimen materials should be 9 : 1. The electric fields $\vec{\mathbf{E}}_{T-Sl}$, $\vec{\mathbf{E}}_P$, $\vec{\mathbf{E}}_{P-Sl}$ and $\vec{\mathbf{E}}_{Sl}$ all remain constant as samples S_1 and S_2 are scanned since these particular electric fields are not transmitted through the superlens. Furthermore, for the sake of simplicity, electric fields $\vec{\mathbf{E}}_{P-Sl-Sa}$ and $\vec{\mathbf{E}}_{Sl-Sa}$ are also assumed to be constant since they reflect in an average manner provided that the width D of sample S_2 is sufficiently small. Therefore, the only electric field affected by the sample pattern is $\vec{\mathbf{E}}_{T-Sl-Sa}$.

In the following analysis, it is assumed that the amplitude of the near-field DC term, $E_{T-Sl}^{0\omega_0}$, has a value of 1.2, while the amplitude of the tip vibration, A, is equal to 60 nm. Furthermore, the higher-order amplitudes are given ideally by $E_{T-Sl}^{n\omega_0} = E_{T-Sl}^{0\omega_0}/2n$ [18], as determined from a Fourier analysis of $E_i\alpha_{eff-1}$. In addition, the incident angle of the light beam is assumed to be $\theta = \pi/6$ and the amplitude of the background electric field is assigned a value of $E_{(Sl)+(Sl-Sa)} = 10$. The amplitudes of the direct probe scattering field, E_P, and reflected field, $E_{(P-S)l+(P-Sl-Sa)}$, are specified as 0.05 and 0.5, respectively, while the phase differences ψ_1, ψ_2, $\phi_R - \phi_{T-Sl}$, and $\phi_R - \phi_{T-Sl-Sa}$ are all assumed to be equal to $\pi/4$. The basic simulation parameters are specified as given in [17]. Finally, $K \sin(\theta)Z_0$ is assigned a value of 0.034 at an incident wavelength of 11 µm. Note that the simulation results obtained using the settings described above are representative of the results obtained using all reasonable parameter settings.

Figure 3 shows the simulation results obtained for the variation of the signal intensity contrast $|S_1/S_2|$ with the transmission coefficient $T(K_{x(T-Sl)}, \lambda)$ at various orders of the radian frequency. As discussed above, the ideal signal intensity contrast, i.e., $|S_1/S_2|_n = \left|I_{n\omega_0(S_1)}/I_{n\omega_0(S_2)}\right| \cong \left|E_{T-Sl(S_1)}^{n\omega_0}/E_{T-Sl(S_2)}^{n\omega_0}\right|$, should be equal to 9 : 1. However, it is evident that none of the intensity contrast profiles approach this ideal value. It is observed that the signal contrast improves with an increasing transmission coefficient $T(K_{x(T-Sl)}, \lambda)$ at all values of the radian frequency order since a higher evanescent wave transmission coefficient results in a better superlens performance. (It should be noted, however, that the incident wavelength λ must induce the superlens effect if the A-SNOM/superlens system is to be able to distinguish between samples S_1 and S_2). Furthermore, it can be seen that the signal contrast improves with an increasing radian frequency
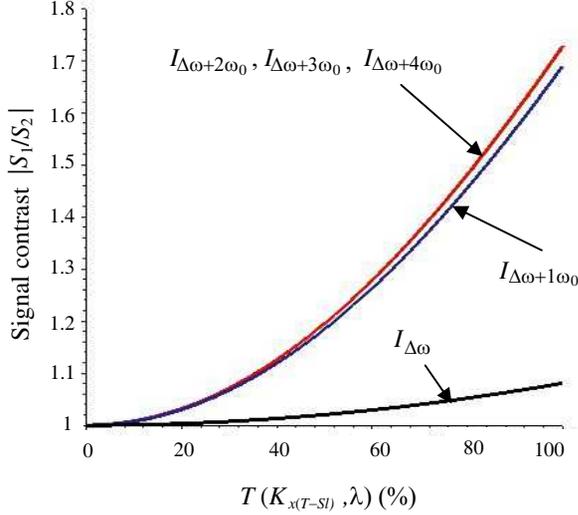
Figure 3. Variation of heterodyne signal contrast with transmission coefficient $T(K_{x(T-Sl)}, \lambda)$ at various radian frequency orders, $\Delta\omega + n\omega_0$.

order [17, 18]. However, as commented above, the signal intensity contrast is still far removed from the ideal value of 9 : 1, even when the transmission coefficient $T(K_{x(T-Sl)}, \lambda)$ increases to a value close to 100%. This result is to be expected since in the experimental method used in [16], and replicated in the simulation results presented in Fig. 3, the tip-superlens interaction electric field, $\vec{\mathbf{E}}_{T-Sl}$, is not removed at any radian frequency order. In other words, $\vec{\mathbf{E}}_{T-Sl}$, represents a source of background noise within the A-SNOM system and therefore reduces the signal contrast.

It has been shown that the resolution of a superlens is strongly suppressed even for small absorption [19]. Moreover, $SiO_2/SiC/SiO_2$ superlenses of the form used in [16] have a spatial resolution of around $\lambda/8$ [26]. In other words, the maximum attainable resolution of an A-SNOM with a superlens is limited principally by that of the superlens. Therefore, in the experimental A-SNOM/superlens system considered in [16], the spatial resolution was found to be just 540 nm, i.e., significantly poorer than that of a conventional A-SNOM system in the mid-infrared range (i.e., ~ 20 nm [20]). The analytical results presented in Fig. 3 relate to a general superlens with transmission coefficient $T(K_{x(T-Sl)}, \lambda)$ rather than the specific $SiO_2/SiC/SiO_2$ superlens considered in [16], but show that the detection signal suffers a signal contrast problem; a fact which was not explicitly discussed

in previous experiments [16]. It is inferred that the non-ideal image contrast shown in Fig. 3 is the result of background noise within the A-SNOM/composite superlens/sample system. Thus, in the following section, a background noise compensation method is proposed for improving the signal contrast in A-SNOM systems with a superlens or composite superlens/sample.

5. BACKGROUND NOISE COMPENSATION METHOD

As described in the previous section, the tip-superlens interaction electric field, $\vec{\mathbf{E}}_{T-Sl}$, acts as background noise within the A-SNOM system, and therefore reduces the signal contrast. The key reason for worst signal contrast is that the two electric fields $\vec{\mathbf{E}}_{T-Sl}$ and $\vec{\mathbf{E}}_{T-Sl-Sa}$, which are extracted simultaneously in the signal processing scheme, both come from α_{eff-1} in A-SNOM heterodyne detection and have the same frequency features. However, the electric field, $\vec{\mathbf{E}}_{T-Sl}$, is not the real sample signal, and must therefore be removed in order to improve the signal contrast. In the present study, this is achieved using the following step-by-step background noise compensation method: (1) measure the superlens signal intensities in the A-SNOM at every radian frequency order without the sample in the system; (2) introduce the sample into the system and re-measure the signal intensities at every radian frequency order; and (3) subtract the intensities obtained in the first step from the equivalent intensities obtained in the second step. The signal intensities at every radian frequency order are therefore obtained as

$$I_{het}(t) = E_R^2 \dots DC$$
$$+2\alpha_{eff-2}T^2(K_{x(T-S)}, \lambda)E_{T-Sl}^{0\omega_0}E_R \cos(\phi_R - \phi_{T-Sl} + \Delta\omega t)$$
$$2E_R E_{P-Sl-Sa}J_0(2\psi_3)\cos(\Delta\omega t + \psi_2)$$
$$+2E_{Sl-Sa}E_R \cos(\phi_R - \phi_{Sl-Sa} + \Delta\omega t)\dots\dots\Delta\omega t$$
$$+4E_R E_{P-Sl-Sa}J_1(2\psi_3)\cos(\omega_0 t)\sin(\Delta\omega t + \psi_2)$$
$$+2\alpha_{eff-2}T^2(K_{x(T-Sl)}, \lambda)E_{T-S}^{1\omega_0}E_R$$
$$\cos(\omega_0 t)\cos(\phi_R - \phi_{T-Sl-Sa} + \Delta\omega t)\dots\dots(\Delta\omega \pm 1\omega_0)t$$
$$-4E_R E_{P-Sl-Sa}J_2(2\psi_3)\cos(2\omega_0 t)\cos(\Delta\omega t + \psi_2)$$
$$+2\alpha_{eff-2}T^2(K_{x(T-Sl)}, \lambda)E_{T-Sl}^{2\omega_0}E_R \cos(2\omega_0 t)$$
$$\cos(\phi_R - \phi_{T-Sl-Sa} + \Delta\omega t)\dots(\Delta\omega \pm 2\omega_0)t$$
$$-4E_R E_{P-Sl-Sa}J_3(2\psi_3)\cos(3\omega_0 t)\sin(\Delta\omega t + \psi_2)$$
$$+2\alpha_{eff-2}T^2(K_{x(T-Sl)}, \lambda)E_{T-Sl}^{3\omega_0}E_R \cos(3\omega_0 t)$$

$$\cos(\phi_R - \phi_{T-Sl-Sa} + \Delta\omega t)\ldots(\Delta\omega \pm 3\omega_0)t$$

$$+4E_R E_{P-Sl-Sa} J_4(2\psi_3)\cos(4\omega_0 t)\cos(\Delta\omega t + \psi_2)$$

$$+2\alpha_{eff-2} T^2(K_{x(T-Sl)},\lambda) E_{T-Sl}^{4\omega_0} E_R$$

$$\cos(4\omega_0 t)\cos(\phi_R - \phi_{T-Sl-Sa} + \Delta\omega t)\ldots(\Delta\omega \pm 4\omega_0)t$$

$$+2E_R E_{P-Sl-Sa}\left\{2\sum_{j=3}^{\infty}(-1)^j J_{2j}(2\psi_3)\cos(2j\omega_0 t)\cos(\Delta\omega t + \psi_2)\right.$$

$$\left.+2\sum_{j=2}^{\infty}(-1)^j J_{2j+1}(2\psi_3)\cos[(2j+1)\omega_0 t]\sin(\Delta\omega t + \psi_2)\right\}$$

$$+2\sum_{n=5}^{\infty}\alpha_{eff-2} T^2(K_{x(T-Sl)},\lambda) E_{T-Sl}^{n\omega_0} E_R \cos(n\omega_0 t)$$

$$\cos(\phi_R - \phi_{T-Sl-Sa} + \Delta\omega t) \tag{21}$$

It is noted that the signal intensities in Eq. (21) are simpler than those in Eq. (20) since the background electric fields $\vec{\mathbf{E}}_{T-Sl}$, $\vec{\mathbf{E}}_P$ and $\vec{\mathbf{E}}_{P-Sl-Sa}$ are all canceled out via the background noise compensation scheme. Significantly, Eq. (21) is also simpler than that proposed by the current group in [18] for conventional heterodyne A-SNOM systems. However, it should be noted that the phases differences between the reference beam and the background signals must remain constant throughout the step (1) and step (2) processes if the electric fields $\vec{\mathbf{E}}_{T-Sl}$, $\vec{\mathbf{E}}_P$ and $\vec{\mathbf{E}}_{P-Sl-Sa}$ are to be completely subtracted.

Adopting the same parameter settings as those used in Section 4 other than $\vec{\mathbf{E}}_{P-Sl-Sa} = 0.25$ (i.e., half the value of $E_{(P-Sl)+(P-Sl-Sa)}$), Fig. 4 shows the signal contrast improvement obtained when using the proposed background noise compensation method. Compared to the results presented in Fig. 3, it can be seen that the signal contrast at higher radian frequency orders is far closer to the ideal value of 9 : 1 even at low values of the evanescent wave transmission coefficient $T(K_{x(T-Sl)},\lambda)$. In practice, this performance improvement arises since the high-order background noise decreases more rapidly than the high-order Bessel functions. As discussed in [17, 18], the discontinuities in the signal contrast profiles $I_{\Delta\omega+2\omega_0}$ and $I_{\Delta\omega+3\omega_0}$ are the result of intensity zero points. Fig. 5 shows the variation of the heterodyne signal intensity with the transmission coefficient $T(K_{x(T-Sl)},\lambda)$ for sample S_1. The results show that the signal intensity reduces with a higher radian frequency order. In other words, the signal extraction process becomes more challenging as the radian frequency order increases.
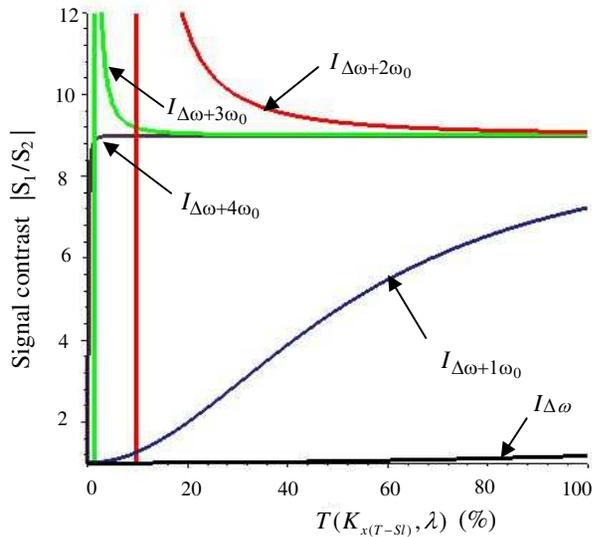
Figure 4. Variation of heterodyne signal contrast with transmission coefficient $T(K_{x(T-Sl)}, \lambda)$ at various radian frequency orders $\Delta\omega + n\omega_0$ when using background noise compensation method.
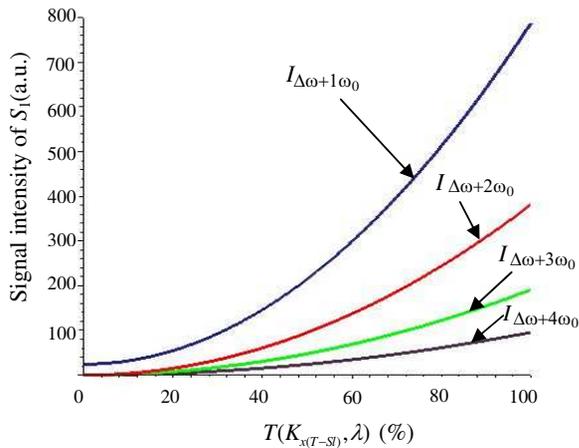

Figure 5. Variation of heterodyne signal intensity with transmission coefficient $T(K_{x(T-Sl)}, \lambda)$ at various radian frequency orders $\Delta\omega + n\omega_0$ when using background noise compensation method.

6. EFFECT OF SUPERLENS ENHANCEMENT IN IMPROVING S/B RATIO AND SIGNAL INTENSITY

Superlenses are generally made of a material with a negative refractive index and are characterized by a negative electric permittivity and magnetic permeability [8–10]. Although quasi-electrostatic theory does not correctly describe tip-superlens enhancement when the permittivity is equal to −1, the electric resonance phenomenon in a superlens results in a very strong tip-superlens enhancement electric field. Provided that this electric field can be transmitted by the superlens, the resulting enhancement electric field between the superlens and the sample may be stronger than the bare tip-sample interaction electric field [31]. In simulating this enhancement effect using the analytical model proposed in this study, an assumption is made that the electric field between the superlens and the sample is 10 times stronger than that between the sample and a bare tip because of the superlens confinement effect [31]. From Fig. 4 in Ref. [31], it had shown that the intensity ($\propto E^2$) between the superlens and sample is at least two orders larger than that between the bare tip and sample. All the remaining parameter settings are identical to those used in Sections 4 and 5.

Figure 6 shows the variation of the heterodyne S/B ratio with the modulation depth ψ_3 at various radian frequency orders for the case of an A-SNOM system with a bare tip only. In general, the S/B ratio can be defined as

$$(S/B)_{Radian\ Frequency\ Order} = |Signal\ Intensity|$$
$$/|Background\ Intensity|_{Radian\ Frequency\ Order}, \qquad (22)$$

where *Signal Intensity* is the term which interacts with the sample at every radian frequency order in Eqs. (20) and (21) and *Background Intensity* is the sum of the other terms. The results presented in Fig. 6 show that the S/B ratio improves with a smaller modulation depth and a higher radian frequency order. Fig. 7 shows the simulation results for the variation of the heterodyne S/B ratio with the modulation depth ψ_3 at various radian frequency orders for the case in which the tip-superlens enhancement effect is taken into account and the background noise compensation method is applied. It is observed that the superlens and noise compensation scheme yield a significant improvement in the S/B ratio and hence in the lateral resolution of the A-SNOM system. In addition, the superlens has a flat surface, and thus in contrast to traditional A-SNOM systems [18], the image obtained during the scanning process has no image artifacts or errors.

The stronger enhancement electric field of an A-SNOM system fitted with a superlens [26] render the A-SNOM/superlens system
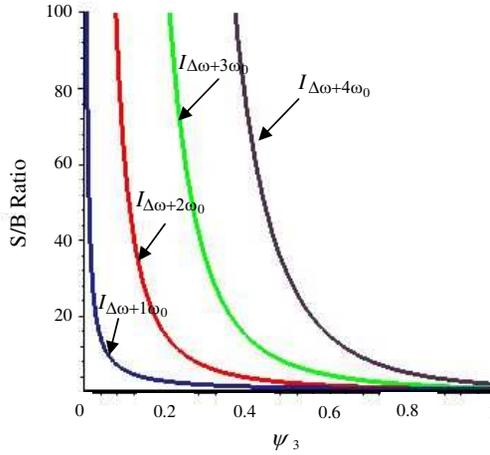
Figure 6. Variation of heterodyne S/B ratio with modulation depth ψ_3 at various radian frequency orders $\Delta\omega + n\omega_0$ in A-SNOM system with bare tip only.
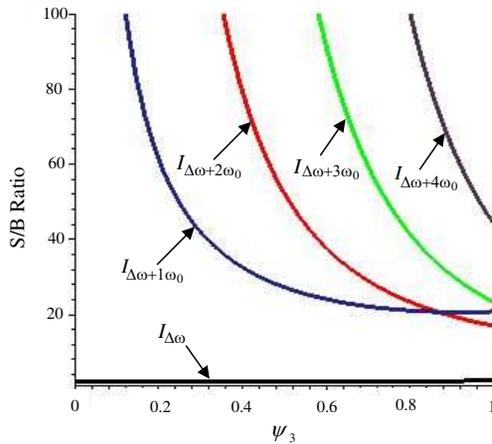

Figure 7. Variation of heterodyne S/B ratio with modulation depth ψ_3 at various radian frequency orders $\Delta\omega + n\omega_0$ in A-SNOM with superlens and background noise compensation method.

a suitable candidate for high-precision nanolithography applications. Figs. 8 and 9 show the simulation results obtained for the variation of the heterodyne signal intensity with the modulation depth ψ_3 as a function of the radian frequency order for in conventional A-SNOM
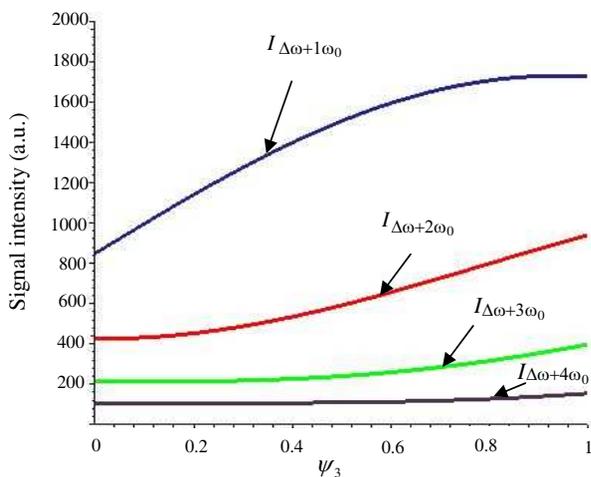
Figure 8. Variation of heterodyne signal intensity with modulation depth ψ_3 at various radian frequency orders $\Delta\omega + n\omega_0$ in A-SNOM system with bare tip only.
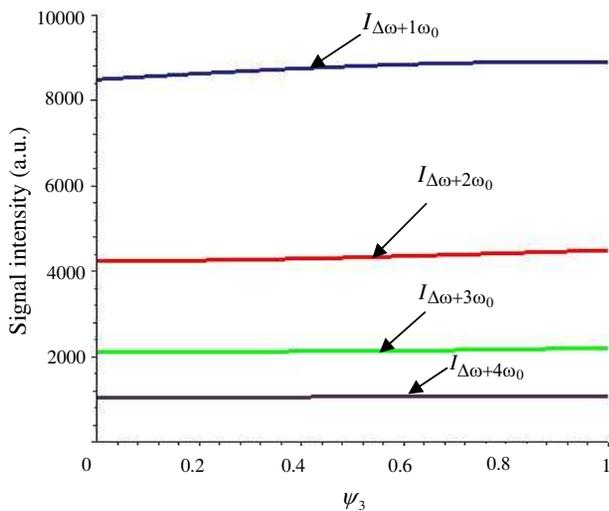

Figure 9. Variation of heterodyne signal intensity with modulation depth ψ_3 at various radian frequency orders $\Delta\omega + n\omega_0$ in A-SNOM system with superlens and background noise compensation method.

and in an A-SNOM/superlens system with the noise compensation scheme, respectively. Comparing the two figures, it can be seen that the signal intensity of the A-SNOM with a superlens and the background noise compensation method is around 10 times higher than that of the conventional A-SNOM with no superlens. As a result, both the total intensity and the S/B ratio of the near-field signal are larger than those in the A-SNOM system with a bare tip only. A-SNOM based nanolithography is traditionally accomplished using a bare tip [32, 33]. However, the analytical results presented in this study Figs. $6 \sim 9$ suggest that an A-SNOM system fitted with a superlens represents a more suitable approach for nanolithography applications due to its better intensity and signal-to-background contrast properties.

7. CONCLUSION

This study has developed an analytical interference-based model for analyzing the detection signals obtained in a reflective-type A-SNOM system with a superlens at various harmonics of the AFM tip vibration frequency. The image resolution is determined not only by the tip radius but also by the superlens transmission coefficient in high wave vector K_x. The analytical results have shown that the tip-superlens interaction electric field represents a major source of background noise within the A-SNOM/superlens system, and therefore results in a significant reduction in the signal contrast. Therefore, a simple background noise compensation method has been proposed for eliminating the effects of the tip-superlens interaction electric field. It has been shown that the proposed compensation scheme results in a significant improvement in both the total intensity and the S/B ratio of the near-field signal in the A-SNOM/superlens imaging system. Consequently, it has been suggested that an A-SNOM system with a superlens represents a more suitable solution for high-precision nanolithography applications than the traditional A-SNOM method. However, this system in nanolithography may have poor lateral resolution because of the poor superlens transmission coefficient in the high evanescent wave vector K_x.

REFERENCES

1. Betzig, E. and M. Isaacson, "Collection mode near-field scanning optical microscopy," *Appl. Phys. Lett.*, Vol. 51, 2088–2090, 1987.

2. Betzig, E., J. K. Trautman, T. D. Harris, J. S. Weiner, and R. L. Kostelak, "Breaking the diffraction barrier-optical microscopy on a nanometric scale," *Science*, Vol. 251, 1468–1470, 1991.

3. Kirstein, S., "Scanning near-field optical microscopy," *Current Opinion in Colloid & Interface Science*, Vol. 4, 256–264, 1999.

4. Hillenbrand, R. and F. Keilmann, "Complex optical constants on a subwavelength scale," *Phys. Rev. Lett.*, Vol. 85, 3029–3032, 2000.

5. Knoll, B. and F. Keilmann, "Enhanced dielectric contrast in scattering-type scanning near-field optical microscopy," *Opt. Commun.*, Vol. 182, 321–328, 2000.

6. Hillenbrand, R., T. Taubner, and F. Keilmann, "Phonon-enhanced light-matter interaction at the nanometer scale," *Nature*, Vol. 418, 159–162, 2002.

7. Novotny, L., E. Z. Sanchez, and X. S. Xie, "Near-field optical imaging using metal tips illuminated by higher-order Hermite-Gaussian beams," *Ultramicrosc*, Vol. 71, 21–29, 1998.

8. Pendry, J. B., "Negative refraction makes a perfect lens," *Phys. Rev. Lett.*, Vol. 85, 3966–3969, 2000.

9. Smith, D. R., J. B. Pendry, and M. C. K. Wiltshire, "Metamaterial and negative refractive index," *Science*, Vol. 305, 788–792, 2004.

10. Shalaev, V. M., "Optical negative-index metamaterials," *Nat. Photonics*, Vol. 1, 41–48, 2007.

11. Wang, G., Y. Gong, and H. Wang, "On the size of left-handed material lens for near-field target detection by focus scanning," *Progress In Electromagnetics Research*, Vol. 87, 345–361, 2008.

12. Wang, R., J. Zhou, C. Sun, L. Kang, Q. Zhao, and J. Sun, "Left-handed materials based on crystal lattice vibration," *Progress In Electromagnetics Research Letters*, Vol. 10, 145–155, 2009.

13. Srivastava, R., S. Srivastava, and S. P. Ojha, "Negative refraction by photonic crystal," *Progress In Electromagnetics Research B*, Vol. 2, 15–26, 2008.

14. Fang, N., Z. Liu, T. J. Yen, and X. Zhang, "Regenerating evanescent waves from a silver superlens," *Opt. Express*, Vol. 11, 682–687, 2003.

15. Fang, N., H. Lee, C. Sun, and X. Zhang, "Sub-diffraction-limited optical imaging with a silver superlens," *Science*, Vol. 308, 534–

537, 2005.

16. Taubner, T., D. Korobkin, Y. Urzhumov, G. Shvet, and R. Hillenbrand, "Near-field microscopy through a SiC superlens," *Science*, Vol. 313, 1595, 2006.

17. Chuang, C. H. and Y. L. Lo, "Analytical analysis of modulated signal in apertureless scanning near-field optical microscopy," *Opt. Express*, Vol. 15, 15782–15796, 2007.

18. Chuang, C. H. and Y. L. Lo, "An analysis of heterodyne signals in apertureless scanning near-field optical microscopy," *Opt. Express*, Vol. 16, 17982–18003, 2008.

19. Podolskiy, V. A. and E. E. Narimanov, "Near-sighted superlens," *Opt. Lett.*, Vol. 30, 75–77, 2005.

20. Ocelic, N., A. Huber, and R. Hillenbrand, "Pseudoheterodyne detection for background-free near-field spectroscopy," *Appl. Phys. Lett.*, Vol. 89, 101124, 2006.

21. Sun, J., P. S. Carney, and J. C. Schotland, "Strong tip effect near-field scanning optical tomography," *J. Appl. Phys.*, Vol. 102, 103103, 2007.

22. Jackson, J. D., *Classical Electrodynamics*, Wiley, 1999.

23. Lee, K., H. Park, J. Kim, G. Kang, and K. Kim, "Improved image quality of a Ag slab near-field superlens with intrinsic loss of absorption," *Opt. Express*, Vol. 16, 1711–1718, 2008.

24. Fujii, M., W. Freude, and J. Leuthold, "Numerical prediction of minimum sub-diffraction-limit image generated by silver surface plasmon lenses," *Opt. Express*, Vol. 16, 21039–21052, 2008.

25. Veselago, V., L. Braginsky, V. Shklover, and C. Hafner, "Negative refractive index materials," *J. Comput. Theor. Nanosci.*, Vol. 3, 1–30, 2006.

26. Korobkin, D., Y. Urzhumov, and G. Shvet, "Enhanced near-field resolution in midinfrared using metamaterials," *J. Opt. Soc. Am. B*, Vol. 23, 468–478, 2006.

27. Smith, D. R., D. S. Schurig, M. Rosenbluth, S. Schultz, S. A. Ramarkrishna, and J. B. Pendry, "Limitations on sub diffraction imaging with a negative index slab," *Appl. Phys. Lett.*, Vol. 82, 1506–1508, 2003.

28. Stefanon, I., S. Blaize, A. Bruyant, S Aubert, G. Lerondel, R. Bachelot, and P. Royer, "Heterodyne detection of guided waves using a scattering-type scanning near-field optical microscope," *Opt. Express*, Vol. 13, 5553–5564, 2005.

29. Lo, Y. L. and C. H. Chuang, "New synthetic-heterodyne demodulation for an optical fiber interferometry," *J. Quantum*

Electron., Vol. 37, 658–663, 2001.

30. Walford, J. N., J. A. Porto, R. Carminati, J. J. Greffet, P. M. Adam, S. Hudlet, J. L. Bijeon, A. Stashkevich, and P. Royer, "Influence of tip modulation on image formation in scanning near-field optical microscopy," *J. Appl. Phys.*, Vol. 89, 5159–5169, 2001.

31. Bortchagovsky, E. G., "Superlens approach to a long-focus near-field probe," *Opt. Lett.*, Vol. 33, 1765–1767, 2008.

32. H'dhili, F., R. Bachelot, G. Lerondel, D. Barchiesi, and P. Royer, "Near-field optics: Direct observation of the field enhancement below an apertureless probe using a photosensitive polymer," *Appl. Phys. Lett.*, Vol. 79, 4019–4021, 2001.

33. Tseng, A. A., "Recent developments in nanofabrication using scanning near-field optical microscope lithography," *Opt. Laser Technol.*, Vol. 39, 514–526, 2007.